Jérôme Boudet[1]
LMFA, UMR CNRS 5509,
Ecole Centrale de Lyon,
Université de Lyon,
Ecully Cedex 69134, France
e-mail: jerome.boudet@ec-lyon.fr

Adrien Cahuzac
LMFA, UMR CNRS 5509,
Ecole Centrale de Lyon,
Université de Lyon,
Ecully Cedex 69134, France

Philip Kausche
Abteilung Triebwerksakustik,
Institut für Antriebstechnik,
Deutsches Zentrum für Luft-und
Raumfahrt (DLR),
Berlin 10623, Germany

Marc C. Jacob
LMFA, UMR CNRS 5509,
Université Lyon 1,
Université de Lyon,
Ecully Cedex 69134, France

Zonal Large-Eddy Simulation of a Fan Tip-Clearance Flow, With Evidence of Vortex Wandering

The flow in a fan test-rig is studied with combined experimental and numerical methods, with a focus on the tip-leakage flow. A zonal RANS/LES approach is introduced for the simulation: the region of interest at tip is computed with full large-eddy simulation (LES), while Reynolds-averaged Navier–Stokes (RANS) is used at inner radii. Detailed comparisons with the experiment show that the simulation gives a good description of the flow. In the region of interest at tip, a remarkable prediction of the velocity spectrum is achieved, over about six decades of energy. The simulation precisely captures both the tonal and broadband contents. Furthermore, a detailed analysis of the simulation allows identifying a tip-leakage vortex (TLV) wandering, whose influence onto the spectrum is also observed in the experiment. This phenomenon might be due to excitation by upstream turbulence from the casing boundary layer and/or the adjacent TLV. It may be a precursor of rotating instability. Finally, considering the outlet duct acoustic spectrum, the vortex wandering appears to be a major contribution to noise radiation.
[DOI: 10.1115/1.4028668]

1 Introduction

The development of complex vortical flows in the rotor blade tip regions is a well-known feature of shrouded turbomachines [1]. These vortices are strongly involved in the issues an aerodynamic designer must address:

(1) losses, associated with shear
(2) stability: a relation was shown between the deviation of the TLV and the onset of spike initiated rotating stall [2]
(3) acoustics: the turbulent eddies developing close to the geometric singularity of the blade tip contribute to broadband noise emission [3,4]

As a consequence, over the past decades, a large number of experimental and numerical studies have been dedicated to the investigation and prediction of the tip-clearance flows. Recent experimental studies range from isolated blades (e.g., Ref. [3]) or cascades (e.g., Ref. [5]), up to representative rigs (e.g., Ref. [6]). Regarding numerical simulations, averaged methods (RANS) are currently widespread in the industry and have shown good capabilities in predicting the mean flow in the tip region [6,7]. However, future progress in aerodynamic design will require an improved modeling of turbulence. For example, the prediction of the acoustic sources requires at least a description of flow spectra and two point correlations. Such an improved description of the unsteady flow can be achieved by LES. A remarkable example of the capabilities of LES is presented by You et al. [8], on a cascade configuration [5]. Application of LES to a rotor configuration was presented by Hah [9] on the NASA Rotor 37, but no detailed experimental data (e.g., spectra) was available to assess the extended description of LES.

This study first aims at introducing a zonal RANS/LES simulation of a fan rotor, where the region of interest at tip is simulated with full LES and the hub and midspan regions are simulated with RANS. The results are compared with new experimental data, including mean flow and spectra downstream of the rotor. Once validated, the simulation is used for an in-depth analysis of the flow, which exhibits a natural unsteadiness.

2 DLR Low-Speed Fan Test Rig

The measurements were performed in a laboratory scale fan rig, at DLR in Berlin. A sketch of the rig is shown in Fig. 1. The main dimensions of the rig and the fan stage are described in Table 1.

Different casing segments can be mounted, for different purposes, e.g., to adjust the rotor tip gap, to evaluate special geometries, to install hot-wire traverses or pressure sensors, and so on. The termination of the exhaust duct is anechoic, with a throttle for setting the operating point.

For the hot-wire measurements, the test rig was equipped with two traverses, marked with white ovals in Fig. 2. Both traverses were equipped with calibrated x-hot-wire probes. The first x-hot-wire probe was at an axial position just upstream of the rotor. The second x-hot-wire probe was located between the rotor and the stator. Both hot-wire traverses have two envelopes. The hot-wire probes can be moved in radial direction and can be rotated, see Fig. 3. The inlet hot-wire probe, upstream of the rotor, was moved in the radial direction only. Downstream of the rotor, the hot-wire probe was also rotated to fit the flow angle of the flow. To get a good impression of the flow field, especially downstream of the rotor, measurements at 40 radial positions between hub and casing were carried out. In comparison to single hot-wire probes, x-wire probes can be used to measure two velocity components of a 3D flow. In the inlet, the x-wire probe was used for the axial and radial components of velocity. Downstream of the rotor, the x-wire probe measured the axial and azimuthal components of velocity. A data acquisition system recorded the data and controlled the traverses automatically. This system also recorded blade and rotor trigger signals. The trigger signals were needed to average the data correctly and even possible variability in the rotation speed.
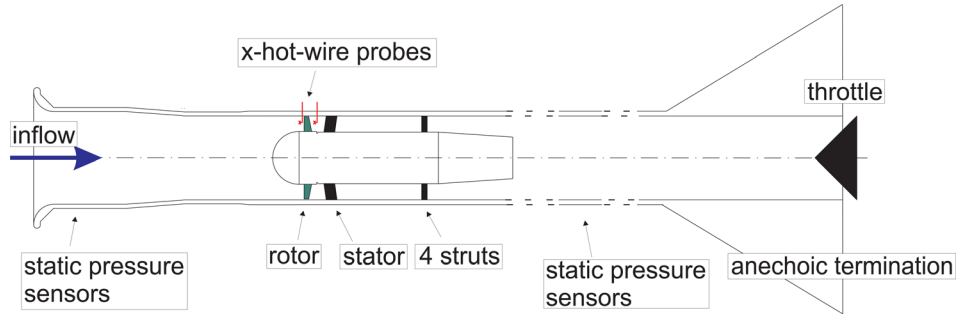
---

[1]Corresponding author.

Fig. 1 Sketch of the DLR fan rig

Table 1 General rig dimensions

Length of inlet duct	$L = 1200\,\text{mm}$
Radius of rotor tip	$R_{\text{tip}} = 226.2\,\text{mm}$
Interstage hub/tip ratio	$\sigma = 0.63$
Rotor blade count	$B = 24$
Stator vane count	$V = 32$
Rotor blade chord length	$c = 43.5\,\text{mm}$
Rotor tip clearance	$s = 2.4\,\text{mm}$
Rotor–stator separation distance (hub/tip)	$g = 37\,\text{mm}/56\,\text{mm}$
Averaged rotor solidity	0.9
Averaged stator solidity	1.5
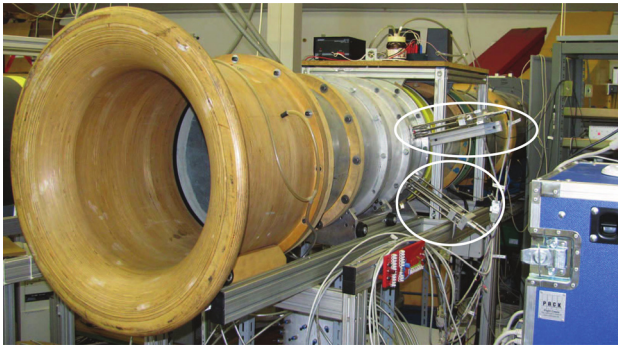
Fig. 2 DLR fan rig with the hot-wire traverses (marked with white ovals)

Fig. 3 Hot-wire probes inside the fan rig duct

In the present study, the rotation speed is set to $\Omega = 3195\,\text{rpm}$, yielding a blade tip Mach number $M_{\text{tip}} = 0.22$ and a Reynolds number $Re = 2.2 \times 10^5$ (based on blade tip velocity and chord length). The mass-flow is adjusted to an intermediate operating point, with a flow coefficient $\phi = 0.24$. In these conditions, the reduced fan loading is $\psi = 0.30$, and the efficiency is 68%. The operating point is shown in the overall performance map of the fan, in Fig. 4, together with the characteristics at $\Omega = 3000\,\text{rpm}$ and various throttle positions (such curves are not available at $\Omega = 3195\,\text{rpm}$). The flow coefficient (ϕ) of the present operating point appears clearly above the value where the efficiency is maximum on the $\Omega = 3000\,\text{rpm}$ characteristic curve. As such, the present operating point is considered as intermediate, in the range of possible flow conditions.

3 Numerical Approach

3.1 Zonal RANS/LES. Undoubtedly, LES offers a deep insight into turbulent phenomena, and yields promising perspectives to aerodynamics. However, in the context of high

Fig. 4 Overall performance of the fan. Δ: reduced fan loading (ψ), $\bigcirc$: efficiency (η). The filled symbols represent the operating condition of the present study ($\Omega = 3195\,\text{rpm}$), while the hollow symbols are for a lower shaft speed ($\Omega = 3000\,\text{rpm}$).

Reynolds number flows, LES involves a large computational cost, often out of reach of current standard capabilities. Consequently, in the literature, a particular attention has been paid to strategies combining RANS and LES modeling, where LES is confined to some regions of the flow. Detached Eddy Simulation [10] is a popular example of such strategies. The approach recently introduced by Tucker et al. [11,12] is an alternative, and has been specifically applied in the context of turbomachines. These two strategies use RANS in the near wall regions, where the grid density requirements of LES are demanding. In the present study, a quite different strategy is employed, described as zonal RANS/LES. Since only the tip-region is of interest, full LES is used for it, down to the wall, while the mid- and low-radius regions are described with RANS. This allows an in-depth analysis of the region of interest, including the inner region of the boundary layers, where the production of turbulence is maximum.

The main equations of RANS and LES (i.e., excluding the turbulence modeling equations) are very similar, even though the variables are mathematically different (RANS: averaged variables, LES: filtered variables). In the context of practical aerodynamic solvers, assuming the grid density is appropriate, the resolution approach (RANS or LES) is essentially controlled by the model viscosity (turbulent viscosity μ_t for RANS, subgrid-scale viscosity μ_{sgs} for LES). Thus, a zonal RANS/LES approach can be expressed on the basis of a common set of equations, which is adjusted locally with a particular attention to the model viscosity

$$\frac{\partial \bar{\rho}}{\partial t} + \frac{\partial \left(\bar{\rho} \widetilde{u}_j \right)}{\partial x_j} = 0 \tag{1}$$

$$\forall i \in 1..3 : \quad \frac{\partial (\bar{\rho} \widetilde{u}_i)}{\partial t} + \frac{\partial \left(\bar{\rho} \widetilde{u}_i \widetilde{u}_j \right)}{\partial x_j}$$
$$= -\frac{\partial \bar{p}}{\partial x_i} + \frac{\partial}{\partial x_j} \left[(\bar{\mu} + \mu_{mod}) \widetilde{\sigma}_{ij} - \frac{2}{3} \bar{\rho} \widetilde{k} \delta_{ij} \right] \tag{2}$$

$$\frac{\partial (\bar{\rho} \widetilde{e}_t)}{\partial t} + \frac{\partial \left[(\bar{\rho} \widetilde{e}_t + \bar{p}) \widetilde{u}_j \right]}{\partial x_j}$$
$$= \frac{\partial}{\partial x_j} \left[(\bar{\mu} + \mu_{mod}) \widetilde{u}_i \widetilde{\sigma}_{ij} - \frac{2}{3} \bar{\rho} \widetilde{k} \widetilde{u}_j \right.$$
$$\left. + c_p \left(\frac{\bar{\mu}}{Pr} + \frac{\mu_{mod}}{Pr_t} \right) \frac{\partial \widetilde{T}}{\partial x_j} + \left(\bar{\mu} + \frac{\mu_{mod}}{\sigma_k} \right) \frac{\partial \widetilde{k}}{\partial x_j} \right] \tag{3}$$

where the overline ($\bar{q}$) denotes the averaging or filtering, the overtilde ($\widetilde{q}$) denotes the Favre decomposition, and

$$\widetilde{\sigma}_{ij} = \frac{\partial \widetilde{u}_i}{\partial x_j} + \frac{\partial \widetilde{u}_j}{\partial x_i} - \frac{2}{3} \delta_{ij} \frac{\partial \widetilde{u}_k}{\partial x_k}$$

The model viscosity μ_{mod} is μ_t in a RANS zone, and μ_{sgs} in a LES zone. Practically, a smooth transition is ensured through a function β

$$\mu_{mod} = (1 - \beta(\mathbf{x})) \mu_{sgs} + \beta(\mathbf{x}) \mu_t \tag{4}$$

where the expression of $\beta(\mathbf{x})$ must be defined a priori, as it controls the zonal cutting of the domain (see Subsection 3.2).

The RANS turbulent viscosity is given by the model of Wilcox [13]

$$\mu_t = C_\mu \bar{\rho} \frac{\widetilde{k}}{\widetilde{\omega}} \tag{5}$$

The LES subgrid-scale viscosity is given by the shear-improved Smagorinsky model [14]

$$\mu_{sgs} = \bar{\rho} (C_s \Delta)^2 \cdot \left(\left| \widetilde{S}(\mathbf{x}, t) \right| - \left| \left\langle \widetilde{S}(\mathbf{x}, t) \right\rangle \right| \right) \tag{6}$$

where S is the strain rate tensor (with: $|S| = (2 \sum_{ij} S_{ij} S_{ij})^{1/2}$), $C_s = 0.18$, and the average $\langle . \rangle$ is computed by exponential smoothing in time [15]. In the present simulation, the cut-off frequency of the smoothing is set at the blade passing frequency ($f_c = 1264$ Hz).

The transport equations for $\widetilde{k}$ and $\widetilde{\omega}$ are solved over the whole domain, in order to close the RANS equations (providing $\widetilde{k}$ and $\widetilde{\omega}$ for Eqs. (1)–(3), and (5)). According to the model of Wilcox

$$\frac{\partial \left(\bar{\rho} \widetilde{k} \right)}{\partial t} + \frac{\partial}{\partial x_j} \left[\bar{\rho} \widetilde{k} \widetilde{u}_j - \left(\bar{\mu} + \frac{\mu_{mod}}{\sigma_k} \right) \frac{\partial \widetilde{k}}{\partial x_j} \right]$$
$$= \left(\mu_{mod} \widetilde{\sigma}_{ij} - \frac{2}{3} \bar{\rho} \widetilde{k} \delta_{ij} \right) \frac{\partial \widetilde{u}_i}{\partial x_j} - C_k \bar{\rho} \widetilde{\omega} \widetilde{k} \tag{7}$$

$$\frac{\partial (\bar{\rho} \widetilde{\omega})}{\partial t} + \frac{\partial}{\partial x_j} \left[\bar{\rho} \widetilde{\omega} \widetilde{u}_j - \left(\bar{\mu} + \frac{\mu_{mod}}{\sigma_\omega} \right) \frac{\partial \widetilde{\omega}}{\partial x_j} \right]$$
$$= C_{\omega 1} \frac{\widetilde{\omega}}{\widetilde{k}} \left(\mu_{mod} \widetilde{\sigma}_{ij} - \frac{2}{3} \bar{\rho} \widetilde{k} \delta_{ij} \right) \frac{\partial \widetilde{u}_i}{\partial x_j} - C_{\omega 2} \bar{\rho} \widetilde{\omega}^2 \tag{8}$$

with the following set of coefficients [13]:

$$C_\mu = 1; \quad \sigma_k = 2.0; \quad \sigma_\omega = 2.0; \quad C_k = 0.09; \quad C_{\omega 1} = \frac{5}{9}; \quad C_{\omega 2} = \frac{3}{40}$$

Finally, in order to recover the LES equations from Eqs. (1)–(3), one should impose $k = 0$ in the LES regions. However, assuming convection between the RANS and LES zones to be negligible (by a proper choice of the zonal cutting), and since the production term of k in Eq. (7) is mostly controlled by μ_{mod}, the value of k computed from Eq. (7) is expected to be small in the LES zones. This is confirmed a posteriori in the present configuration: in the LES region, k is about 1/20th of the kinetic energy of the fluctuations. Consequently, the three terms involving k in Eqs. (1)–(3) are not explicitly set to zero in the LES zones, for practical reasons.

More discussions about the zonal RANS/LES strategy, and a channel flow validation, can be found in Ref. [16].

3.2 Computation Setup. The simulation has been carried out with TURB'FLOW [17], an in-house Navier–Stokes solver dedicated to turbomachines. The equations and the turbulent closure have been presented in Subsection 3.1. The discretization uses finite volumes on multiblock structured grids. Inviscid fluxes are interpolated with a four-point centered scheme, with fourth order numerical viscosity (Jameson [18] coefficient: ≤ 0.01 in the region of interest at tip). Viscous fluxes rely on a two-point centered interpolation. Time resolution is explicit, with a three-step Runge–Kutta method, and the time step is: $2.5 \times 10^{-8} s$ $\approx 2 \times 10^{-5} c / U_Q^{FF}$.

The transition between the RANS zone (low- and mid-radius region) and the LES zone (region of interest at tip) is ensured by a third order polynomial function $\beta(\mathbf{x})$, with

$$\beta(r \leq 0.89 \cdot R_c) = 1 \quad \text{and} \quad \partial \beta / \partial r (r = 0.89 \cdot R_c) = 0$$
$$\beta(r \geq 0.94 \cdot R_c) = 0 \quad \text{and} \quad \partial \beta / \partial r (r = 0.94 \cdot R_c) = 0$$

The computational domain includes a long section of the inlet duct (azimuthal sector: 1.875 deg) and one rotor passage. It is presented in Fig. 5, and the mesh on a meridian sheet is shown. The simulation of the inlet duct section allows the casing boundary layer to develop upstream of the rotor. The grid consists of about 11×10^6 points, distributed in 75 structured blocks. In the LES region at tip, the cell dimensions at the wall are around the classical criteria for LES [19] in wall units: $\Delta x^+ < 30$ (streamwise direction), $\Delta y^+ < 3$ (wall-normal direction), and $\Delta z^+ < 50$ (transverse direction). In the RANS region at inner radii, the spanwise (i.e., radial) dimension is increased up to $\Delta z^+ = 400$.
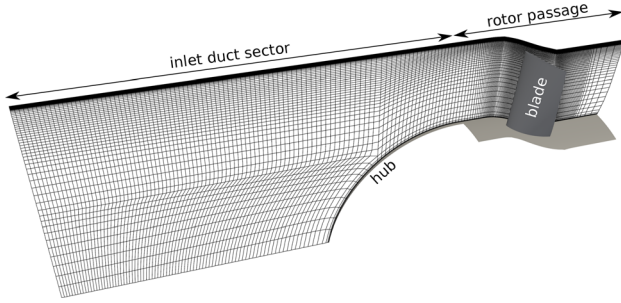
Fig. 5 Computational domain: inlet duct sector and rotor passage. The mesh on a meridian sheet is shown, with every second point plotted in each direction.
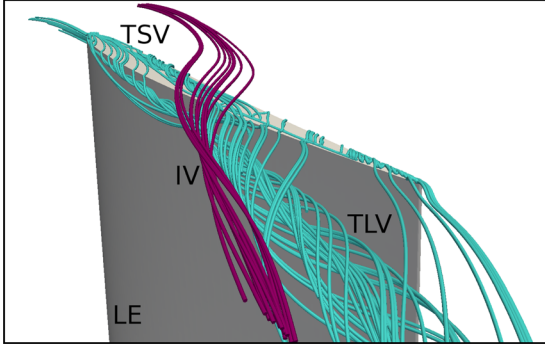

Fig. 7 Mean pressure coefficient on the blade surface, from the simulation. Solid line: midspan; dashed-dotted line: close to the tip at 97% span.

Fig. 6 Streamlines of the LES mean flow in the blade tip region

Fig. 8 Instantaneous isosurface of Q-criterion $(8 \times 10^7 \, s^{-2})$, colored by chordwise vorticity

An adiabatic no-slip condition is specified on the walls. At the inflow, density and velocity are imposed. A particular treatment handles the interface between the inlet duct sector and the rotor passage (see Fig. 5), since the former only covers 1/8th of the azimuthal extent of the latter. There is a direct contact over 1/8th of the rotor passage, and the rest of the rotor face is set as inflow and fed by periodic copies of the inlet duct flow. At the rotor outflow, a sponge layer is designed (smooth coarsening of the mesh and increase of the numerical viscosity), and a semi-non-reflecting condition is used to impose the mean static pressure with a radial equilibrium. The "semi-non-reflecting condition" is a linear combination of an outflow condition (where static pressure is imposed) and a nonreflecting condition. The weight coefficients are, respectively, $0.5(1 - \mathrm{Ma})$ and $0.5(1 + \mathrm{Ma})$, where Ma is the maximum Mach number in the outflow.

The zonal simulation has been initialized from a preliminary under-resolved full-LES computation [20], and then run for a duration of $17 \cdot c/U_Q^{\mathrm{FF}}$ (10^6 iterations) in order to reach statistical stationarity on the numerical probes. Then, the results have been acquired over more than $10 \cdot c/U_Q^{\mathrm{FF}}$ (6.4×10^5 iterations). The computational cost of the complete zonal simulation is 1.4×10^5 central processing unit (CPU) hours.

4 Combined Analysis of the Experimental and Numerical Results

The mean vortical topology of the simulation is illustrated in Fig. 6. Classical structures [8] are observed. The light-blue streamlines reveal the largest vortex, known as tip-leakage vortex (TLV), which results from the interaction of the leakage flow with the main flow through the passage. It is fed around midchord by tip-separation vortices (TSV) that develop on the blade tip edges. The dark purple streamlines originate from the casing boundary layer and are entrained by the induced vortex (IV), which is generated aside the TLV, with an opposite sense of rotation.
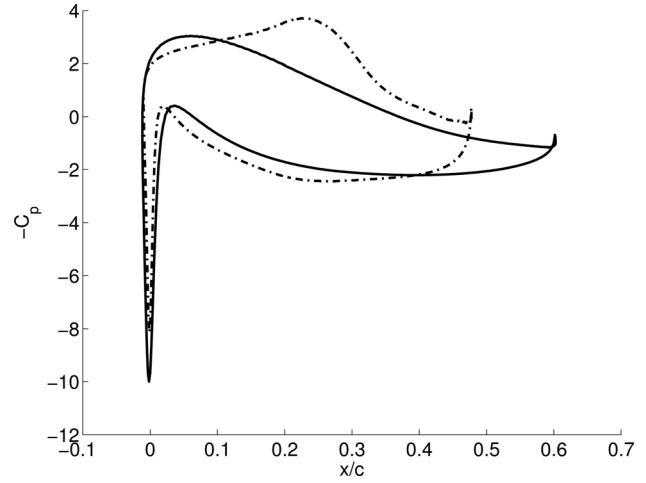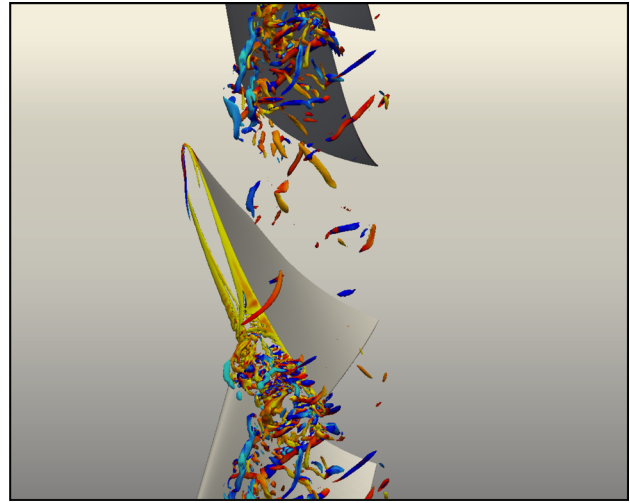
The blade pressure coefficient is plotted in Fig. 7 at midspan and close to the tip. At midspan, the distribution is rather classical for a low-speed fan. Close to the tip, a low-pressure hump is visible on the suction side, because of the influence of the TLV.

The description by LES of the largest turbulent eddies is illustrated in Fig. 8, where the instantaneous vortical flow is presented. Elongated turbulent eddies are observed around the TLV and the IV. Interestingly, some of these eddies are shown to travel from one blade tip to the adjacent one, and to perturb the root of the adjacent TLV. This is particularly observable when this view is animated.

Thereafter, the results of the simulation are analyzed in comparison with the available experimental data. Flow statistics and velocity spectra are examined, using the same postprocessing routines for the experiment and the simulation. Unfortunately, it is not possible to compare the fan characteristics (pressure rise and efficiency) between the experiment and the simulation, since these quantities are extracted for the whole stage (rotor + stator) in the experiment, whereas only the rotor is simulated. However, the rotor performances can be compared through alternative quantities. First, the flow coefficient of the simulation is imposed by the boundary conditions, and is thus equal to the experimental value. Second, the rotor performances will be evaluated and compared
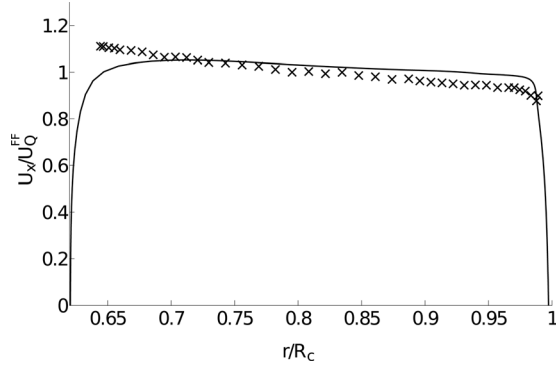
Fig. 9 Radial profile (time and azimuthal average) of axial velocity U_x in the fan face plane. ×: measurements; solid line: simulation.

with the experiment. The main discrepancy is in the hub region, where the simulation yields smaller velocities than the experiment. More precisely, the boundary layer thickness on the hub is significantly overpredicted. When plotting the turbulent kinetic energy k in the intake (not shown here), a region with high values of k is observed along the bullet nose, near the stagnation point. This is a classical flaw of RANS turbulence models [21], and particularly of the present k–ω model. The production of k is overestimated around the leading edges of bodies (here: the bullet nose). In the present computation, the k-production limiter proposed in Ref. [21] is used, but it does not completely suppress the default. This overproduction of k then strengthens the diffusion of the boundary layer and results in an overprediction of the boundary layer thickness.

In the region of interest near the casing, the experiment shows a sudden velocity drop, probably associated with the casing boundary layer. The thickness of this boundary layer appears to be well captured by the simulation.

through the velocity flow maps downstream of the rotor (Figs. 10(c)–10(f)), which enable to characterize the deviation and the velocity deficit regions.

4.1 Mean Flow at the Rotor Fan Face. The radial profile of the mean axial velocity at the fan face, that is, upstream of the fan, is presented in Fig. 9. The simulation is in fair agreement

4.2 Flow Statistics Downstream of the Rotor. The mean velocity components and the turbulent intensity are discussed in this subsection, from the analysis of the experimental and numerical results. First, the relative streamwise velocity is presented in Figs. 10(a) (flow maps) and 10(b) (radial profiles). A fairly good agreement is achieved between the experiment and the simulation. The magnitude of the velocity and the radial gradient are captured
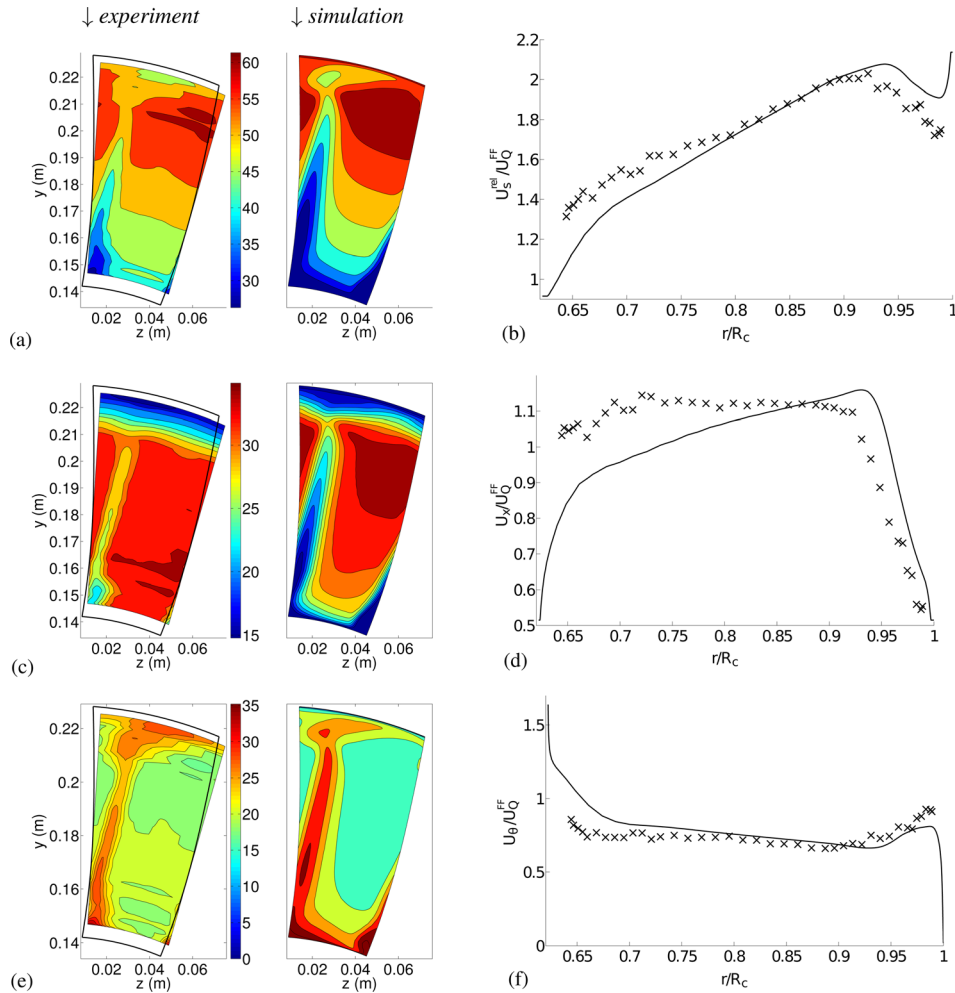

Fig. 10 Mean velocity components downstream of the rotor (computed in the rotating frame of reference). (a), (c), and (e): contours (the simulation domain boundaries are drawn on the experimental maps). (b), (d), and (f): radial profiles (time and azimuthal average). ×: measurements; solid line: simulation.

by the simulation. Also, the velocity deficit at tip, associated with the clearance flow, is fairly well simulated. Considering the radial profiles (Fig. 10(b)) with more attention, the simulation appears to underestimate the velocity in the hub region. The flow maps (Fig. 10(a)) show this is due to an overestimate of the blade wake near the hub. This is consistent with the upstream results at the fan-face, where the simulation shows lower velocities than the experiment in the hub region. However, the attention of this work is focused on the tip-region, where the clearance flow results in a velocity deficit. The radial extent of the velocity deficit region is correctly simulated, and the velocity is overestimated by roughly 9% (according to Fig. 10(b)), as a consequence of the blockage in the hub region. On the whole, the description of the tip-region by the simulation is fairly good.

The mean axial velocity is presented in Figs. 10(c) and 10(d), and the tangential velocity in Figs. 10(e) and 10(f). The discrepancies previously observed on the relative streamwise velocity mainly affect the axial velocity: the blade wake is overestimated in the hub region, the radial extent of the clearance flow is correctly captured (compare the radii of the velocity drop in Fig. 10(d)), but the velocity is overestimated at tip because of the blockage in the hub region. Concerning the tangential velocity, a good agreement is observed between the experiment and the simulation. The radial profile is nearly uniform, except in the hub and tip regions, where the tangential velocity increases in relation with the reduction of the axial velocity. These evolutions and the velocity magnitudes are correctly simulated.

The turbulent intensity of the fluctuations is shown in Figs. 11(a) and 11(b). This quantity is computed as

$$Tu_{\text{fluc}} = \frac{\sqrt{\frac{1}{3}\left(u_x'^2 + u_y'^2 + u_z'^2\right)}}{U_s} \tag{9}$$

where u_x', u_y', and u_z' are the root-mean squared velocity fluctuations, and U_s is the local mean streamwise velocity. For the simulation, it is important to notice that Tu_{fluc} only represents the turbulent intensity in the LES region (i.e., near the casing). In the RANS region, the turbulent intensity must be computed from the variable k. However, the definition of a unified turbulence intensity (valid both in the RANS and LES regions) is not trivial, essentially because the equation of k is also solved in the LES region but not used to compute μ_{mod}. Consequently, only Tu_{fluc} is presented here. This quantity is representative of the turbulent intensity in the region of interest near the casing. The clearance flow region is characterized by high values of the turbulent intensity, which are slightly underestimated by the simulation. According to Fig. 11(b), the clearance flow region extends down to $r/R_c \approx 0.88$ in the experiment, and $r/R_c = 0.9$ in the simulation. The value of Tu_{fluc} is not exactly zero in the RANS region
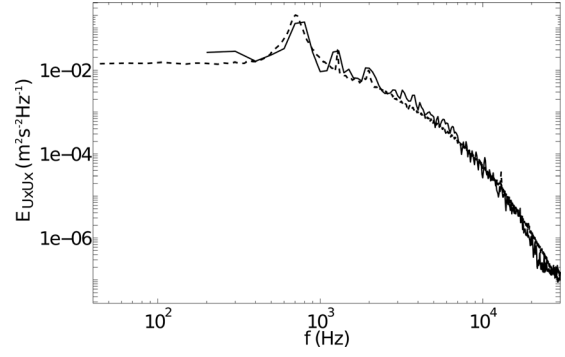
Fig. 12 Power spectral density of the axial velocity, in the downstream plane at radius $r = 0.98\ R_c$. Dashed line: experiment; solid line: simulation.

($r \leq 0.89\ R_c$), because of residual fluctuations, partly induced by the unsteadiness in the nearby LES region.

4.3 Velocity Spectra Downstream of the Rotor. A major added-value of LES with respect to RANS is the description of a large part of the spectral content of the flow. Such an approach is able to predict complex interactions between the mean flow and the large scale turbulent eddies in the time domain, while RANS is limited by its modeling hypotheses and calibrations. The direct description of the largest turbulent eddies also permits to compute directly the broadband noise sources, while RANS requires further modeling approximations. As a consequence, a proper evaluation of LES must consider the spectral content of the flow, which can be here compared to the X-wire measurements downstream of the rotor.

The present study is focused on the tip-flow. Therefore, spectra are extracted at the radial position $r = 0.98\ R_c$, in the static frame of reference. The axial velocity and tangential velocity spectra are presented in Figs. 12 and 13. A remarkable agreement is observed between the experiment and the simulation, for both velocity components. The peak above 10^4 Hz, particularly visible in Fig. 13, corresponds to an eigenfrequency of the hot-wire probe. Therefore, it is not present in the simulation.

The broadband content of the flow is captured over the whole experimental range of frequencies (up to $\sim$20 kHz) and about six decades of energy. This indicates the energy distribution among the large turbulent eddies is correctly reproduced by the LES simulation. This is a notable proof of quality of the computation.

Furthermore, the dominant peaks of the experimental spectra are also captured by the simulation. Three dominant frequencies are particularly visible on the axial velocity spectrum, in Fig. 12: $f_1 = 710$ Hz, $f_2 = 1280$ Hz, and $f_3 = 1980$ Hz (these precise values
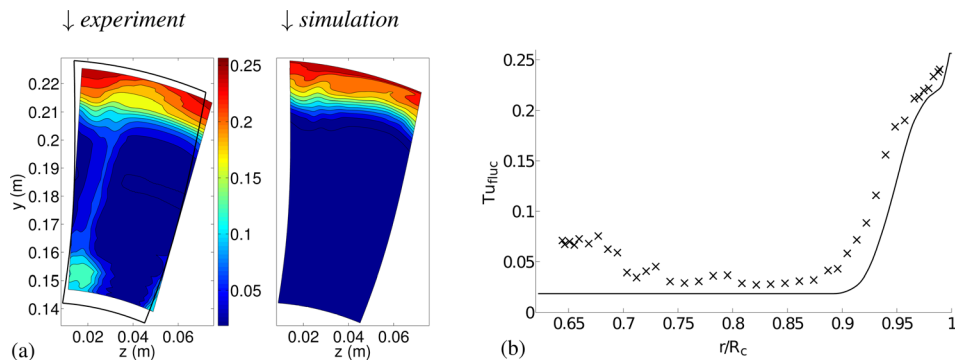

Fig. 11 Turbulence intensity of the fluctuations downstream of the rotor (computed in the rotating frame of reference). (a) contours (the simulation domain boundaries are drawn on the experimental map). (b) radial profiles (time and azimuthal average). ×: measurements; solid line: simulation.
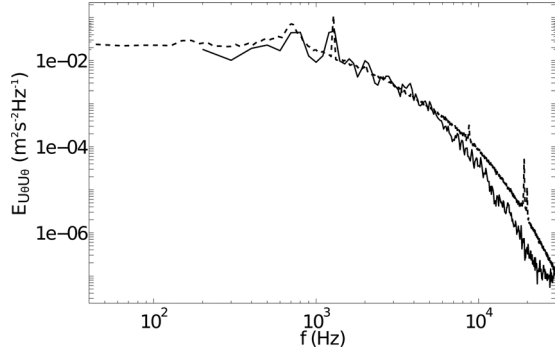
Fig. 13 Power spectral density of the tangential velocity, in the downstream plane at radius $r = 0.98\ R_c$. Dashed line: experiment; solid line: simulation.

are obtained from the experimental spectrum, which has a finer frequency resolution: $\Delta f = 15$ Hz). The f_2 peak corresponds to the blade passing frequency, and represents the influence of the rotor wakes. The other two peaks are clearly related, through nonlinear combination with f_2, since $f_3 = f_1 + f_2$ (by the experimental resolution). The f_1 peak is dominant. It must be associated to a natural unsteadiness, since the blade passing is the only deterministic unsteadiness that can arise in the simulation, at the frequency f_2 and its harmonics. The significant width of the f_1 peak around its central value (see Fig. 12) is another indication of its nondeterministic nature. This feature is further investigated in Sec. 5.

5 Natural Unsteadiness

We call "natural unsteadiness" a turbomachine unsteadiness that is not related to rotor/stator interaction frequencies. According to the literature, various flow phenomena can be classified into this category, such as: rotating stall [22], rotating instabilities [23,24], oscillations of the TLV [25] and vortex shedding.

As pointed out above, the f_1 component observed in Figs. 12 and 13 is most certainly due to a natural unsteadiness, whose physical nature is to be determined. A rotating stall is not expected at this intermediate operating condition (flow coefficient: $\phi = 0.24$). But rotating instabilities have been largely documented on variants of this rig [24,26], in similar regimes.

In the simulation, the axial velocity spectrum can be computed from a rotating probe. The result is presented in Fig. 14, for a probe at $r = 0.98\ R_c$ in the TLV. A peak protrudes at $f = 1800$ Hz, together with harmonics. This must be associated to the natural unsteadiness, since the rotor unsteadiness is the only deterministic unsteadiness in the simulation, and it is not visible in this frame of reference. No rotating-frame measurement is available from the experiment, but acoustic measurements in the outlet duct are presented in Fig. 15. Here again, a dominant peak is visible at
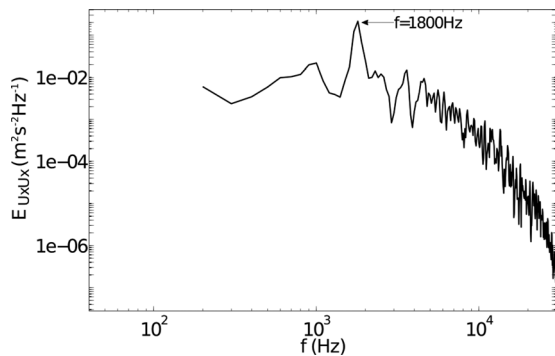

Fig. 14 Simulation: power spectral density of the axial velocity, at a point attached to the rotating frame of reference, in the downstream plane at radius $r = 0.98\ R_c$
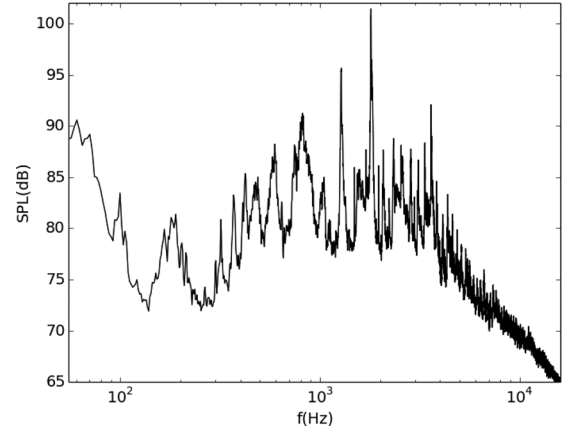

Fig. 15 Experiment: sound pressure spectrum

$f = 1800$ Hz. The 1800 Hz peaks from Figs. 14 and 15 can be related, assuming the Doppler effect to be negligible, since the outlet duct axis is perpendicular to the trajectory of the blades. This hypothesis is supported by the results of Kameier and Neise [26], on a previous version of this rig: coincident frequencies were observed between wall-mounted pressure probes and the acoustic measurements, attributed to tip-clearance noise. Therefore, the simulation peak at $f = 1800$ Hz, in the rotating frame of reference, appears to be confirmed by the experiment. In Fig. 14, the peak is artificially broadened by the coarse frequency resolution of the simulation ($\Delta f \approx 100$ Hz for the averaged spectrum). In Fig. 15, the frequency resolution of the experiment is much finer ($\Delta f = 2$ Hz), and the peak appears sharp. This sharp peak in the acoustic spectrum is not contradictory with the broad peak observed for the near-field velocity (e.g., in Fig. 12). Indeed, acoustic pressure is an integrated value, which averages out local frequency jitter. Moreover, some local aerodynamic fluctuations might not propagate as acoustics. The experimental spectrum in Fig. 15 also shows additional peaks beside the $f = 1800$ Hz peak and the blade passing components. They are probably associated to interactions with the stator vanes, which are not taken into account in the simulation.

The frequency of the natural unsteadiness in the rotating frame of reference, $f = 1800$ Hz, is worth attention. It is higher than the blade passing frequency (in the static frame of reference). This is against the hypothesis of a rotating instability constituted by a number of cells that rotate in a nearly frozen state at its own speed, as described by Kameier and Neise [26] or Inoue et al. [23]. Such rotating instabilities generally have a number of cells smaller than the number of blades, with a rotational speed about half the shaft speed. These conditions do not allow a higher frequency than the blade passing frequency, in the rotating frame of reference, as observed here.

The Fourier transform (in time) of the whole tridimensional flow can be computed from the simulation, in the rotating frame of reference, at the frequency of the natural unsteadiness ($f = 1800$ Hz). The real part of the radial-velocity Fourier transform is plotted in Fig. 16, where positive and negative valued isosurfaces are shown. The highest amplitudes are observed at the blade tip, on the suction side, in the region of the TLV. Therefore, the natural unsteadiness is most certainly associated with the TLV. Furthermore, the alignment of the positive and negative isocontours along the vortex axis, alternating laterally at nearly constant radius, indicates a lateral oscillation of the TLV. Such a phenomenon, called "vortex wandering," has been visualized by Zierke et al. [25], in a high-Reynolds number pump facility. These authors also cite previous observations, concerning tip vortices behind a wing or a hydrofoil. More recently, You et al. [27] detected a wandering of the tip leakage vortex in a cascade configuration, from both experimental and numerical results. These authors calculated the Strouhal number of the oscillation
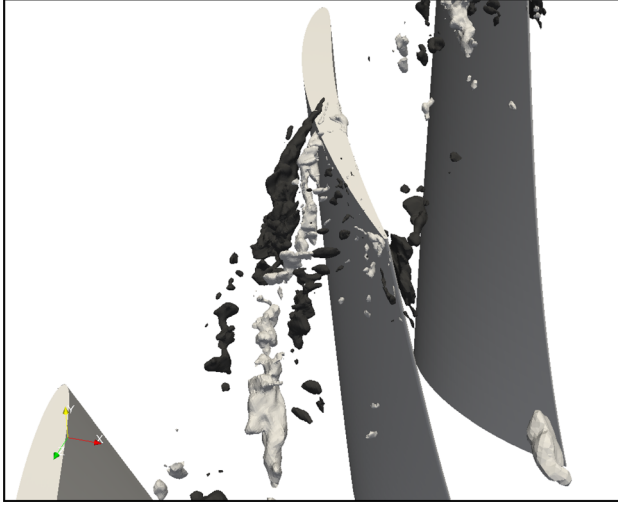
Fig. 16 Real part of the radial velocity Fourier transform ($f = 1800$ Hz): isosurfaces at -4×10^{-6} m/s (dark gray) and 4×10^{-6} m/s (light gray)

(nondimensional frequency, based on the chord length and the upstream velocity): St = 1.5, in the blade vicinity. In the present study, the Strouhal number is computed in the rotating frame of reference, with the upstream relative streamwise velocity at the tip. The value, St = 1.0, is in good agreement with the cascade study. You et al. [27] considered shear-layer instability in the clearance jet flow was the most probable origin of the natural unsteadiness in the cascade configuration. We suggest a different mechanism: the wandering could be a response of the TLV to upstream turbulence. In the present configuration, upstream turbulence is provided by the casing boundary layer and the impact of the adjacent TLV on the blade being considered. Such a response to turbulence has been studied by Bailey and Tavoularis [28], on a wing tip vortex. These authors obtained values of the Strouhal number consistent with the values mentioned above: St $\approx$ 0.5 and 0.3 at distances $4c$ and $6c$ downstream of the blade, respectively (c: chord length).

These arguments tend to demonstrate that the natural unsteadiness observed here is related to a wandering of the TLV. This is not contradictory with the previous studies [24,26], which described rotating instabilities on variants of the same rig, for various operating conditions in the high loading range (i.e., low flow coefficient ϕ). The phenomenon described by these authors is made of flow cells that propagate from one rotor passage to the adjacent one, at an intermediate rotation speed. The present oscillation of the TLV can coexist with the rotating instability. It could even be a precursor of the rotating instability, since it occurs at intermediate loading. This was already suggested by the numerical results of März et al. [24], on a variant of the same rig (different tip gap width, rotor speed and stator geometry). These authors carried out a simulation over the whole circumference of the rotor, with a rather coarse grid, and the mass flow was reduced progressively from a stationary operating point. They observed first a wandering of the TLV, before the rotating instability developed. The following mechanism, from vortex wandering to rotating instability, is proposed. When the flow rate is reduced, the TLV trajectory leans upstream, toward the azimuthal direction, and impacts the adjacent blade. Consequently, a wandering of the TLV results in a quasi-periodic influence on the adjacent passage, which excites the adjacent TLV, and so on, from one passage to the next one. This could generate a perturbation of the tip flow, rotating at its own speed. At the present time, this mechanism is only a hypothesis, and further studies should be carried out to confirm it. Such studies should consider the evolution of the unsteadiness, when reducing the flow coefficient from the present conditions. In the present simulation, the natural frequency does

not appear to be altered by the periodic boundary conditions, probably because vortex wandering affects all the passages. But when reducing the flow coefficient, the whole circumference should be taken into account, in order not to influence the development of the rotating instability. The experiment is particularly adapted to such investigations, and the attention should be focused on the evolution of the frequencies here associated with the vortex wandering. In addition, thanks to the progress of the available computational resources, it is possible to envisage computations like the present one over a full circumference, in order to access the details of the flow when reducing the flow coefficient toward regimes where the rotating instability appears.

Finally, it is remarkable that the frequency associated with the natural unsteadiness ($f = 1800$ Hz) dominates the acoustic spectrum in Fig. 15. The possible mechanisms of noise radiation by vortex wandering can be discussed. While the wandering motion, which is comparable to a low frequency oscillation of the TLV, is not expected to generate a significant amount of noise by itself, it might generate strong sound waves when hitting the tip of the adjacent blade. Moreover, the oscillation modifies the tip-to-vortex distance, thus acting upon the tip or trailing-edge radiation of the blade being considered. The interactions between the vortex wandering, the rotor and the stator can explain the various peaks observed in the measured sound spectrum (Fig. 15). Finally, the low frequency peaks are not due to cascade resonances, which are in the high frequency range (above 2800 Hz).

6 Conclusion

The analysis of the flow in a fan test rig has been carried out by combined experimental and numerical means. On the numerical side, a zonal RANS/LES approach has been introduced, in order to investigate with full LES the tip-flow region, particularly of interest here, while a RANS description is used at inner radii.

Comparison of the experimental and numerical results shows the simulation provides a good description of the flow, with, however, some overestimate of the blade wake near hub. The region of interest, near the casing, is simulated with precision. Remarkable results are obtained on the velocity spectra downstream of the rotor. The tonal and broadband contents of the flow are precisely simulated, over about six decades of energy. This description by LES of the turbulence dynamics in the tip flow is a major achievement of the present work.

Finally, a natural unsteadiness has been detected in both the experimental and numerical spectra. A detailed analysis of the LES results, with Fourier decomposition over the whole domain, indicates a wandering motion of the TLV. The Strouhal number is about unity, in good agreement with previous observations of this phenomenon. We suggest this oscillation could be excited by turbulence from the casing boundary layer and/or the adjacent TLV, and could be a precursor of rotating instability. This natural unsteadiness appears also to dominate the measured sound spectrum, which makes it worth attention during the design process of a fan. Further studies are necessary to investigate the mechanisms and the parameters of this phenomenon, and to provide some design rules to the engineers.

Acknowledgment

Nomenclature

c_p = specific heat at constant pressure
C_p = pressure coefficient (normalized with the fan-face mean values)
IV = induced vortex

k = turbulent kinetic energy
LES = large-eddy simulation
p = static pressure
Pr = Prandtl number
Pr_t = turbulent Prandtl number
Q_v = volume flow rate
r = radius
R_c = casing radius
R_{tip} = rotor tip radius
RANS = Reynolds-averaged Navier–Stokes
T = static temperature
TLV = tip-leakage vortex
Tu_{fluc} = turbulence intensity of the fluctuations
u_x, u_r, u_z = Cartesian components of velocity (eq. u_i, $i = 1\ldots3$)
u_x, u_r, u_θ = axial, radial, and azimuthal velocities
U_Q^{FF} = mean flow velocity at fan face ($= 28.73$ m/s from the simulation)
β = RANS/LES zonal coefficient
ΔP_t = total pressure increase
η = isentropic efficiency of the fan stage (rotor + stator)
μ_{mod} = RANS/LES dynamic viscosity
μ_{sgs} = subgrid-scale viscosity (LES)
μ_t = turbulent viscosity (RANS)
ρ = density
$\phi = Q_v/(\pi\Omega R_{tip}^3)$, flow coefficient
$\psi = \Delta P_t/(0.5\rho\Omega^2 R_{tip}^2)$, reduced fan loading
ω = specific dissipation rate of turbulence
Ω = rotation speed

References

[1] Lakshminarayana, B., 1996, *Fluid Dynamics and Heat Transfer of Turbomachinery*, John Wiley & Sons Inc., Hoboken, NJ.
[2] Vo, H. D., Tan, C. S., and Greitzer, E. M., 2008, "Criteria for Spike Initiated Rotating Stall," ASME J. Turbomach., **130**(1), p. 011023.
[3] Camussi, R., Grilliat, J., Caputi-Gennaro, G., and Jacob, M. C., 2010, "Experimental Study of a Tip Leakage Flow: Wavelet Analysis of Pressure Fluctuations," J. Fluid Mech., **660**, pp. 87–113.
[4] Jacob, M. C., Grilliat, J., Camussi, R., and Caputi Gennaro, G., 2010, "Aeroacoustic Investigation of a Single Airfoil Tip Leakage Flow," Int. J. Aeroacoustics, **9**(3), pp. 253–272.
[5] Muthanna, C., and Devenport, W. J., 2004, "Wake of a Compressor Cascade With Tip Gap, Part 1: Mean Flow and Turbulence Structure," AIAA J., **42**(11), pp. 2320–2331.
[6] Gourdain, N., Wlassow, F., and Ottavy, X., 2012, "Effect of Tip Clearance Dimensions and Control of Unsteady Flows in a Multi-Stage High-Pressure Compressor," ASME J. Turbomach., **134**(5), p. 051005.
[7] Storer, J. A., and Cumpsty, N. A., 1991, "Tip Leakage Flow in Axial Compressors," ASME J. Turbomach., **113**(2), pp. 252–259.
[8] You, D., Wang, M., Moin, P., and Mittal, R., 2007, "Large-Eddy Simulation Analysis of Mechanisms for Viscous Losses in a Turbomachinery Tip-Clearance Flow," J. Fluid Mech., **586**, pp. 177–204.
[9] Hah, C., 2009, "Large Eddy Simulation of Transonic Flow Field in NASA Rotor 37," NASA Glenn Research Center, Cleveland, OH, Technical Report No. TM-2009-215627.
[10] Spalart, P. R., 2009, "Detached-Eddy Simulation," Annu. Rev. Fluid Mech., **41**(1), pp. 181–202.
[11] Tucker, P., Eastwood, S., Klostermeier, C., Jefferson-Loveday, R., Tyacke, J., and Liu, Y., 2012, "Hybrid LES Approach for Practical Turbomachinery Flows—Part I: Hierarchy and Example Simulations," ASME J. Turbomach., **134**(2), p. 021023.
[12] Tucker, P., Eastwood, S., Klostermeier, C., Xia, H., Ray, P., Tyacke, J., and Dawes, W., 2012, "Hybrid LES Approach for Practical Turbomachinery Flows—Part II: Further Applications," ASME J. Turbomach., **134**(2), p. 021024.
[13] Wilcox, D. C., 1993, *Turbulence Modeling for CFD*, DCW Industries, Inc., La Canada, CA.
[14] Lévêque, E., Toschi, F., Shao, L., and Bertoglio, J. P., 2007, "Shear-Improved Smagorinsky Model for Large-Eddy Simulation of Wall-Bounded Turbulent Flows," J. Fluid Mech., **570**, pp. 491–502.
[15] Cahuzac, A., Boudet, J., Borgnat, P., and Lévêque, E., 2010, "Smoothing Algorithms for Mean-Flow Extraction in Large-Eddy Simulation of Complex Turbulent Flows," Phys. Fluids, **22**(12), p. 125104.
[16] Cahuzac, A., 2012, "Aspects Cinétiques et Acoustiques en Simulation Numérique des Grandes Échelles, et Application à L'étude du Controle de l'écoulement de jeu en Turbomachines," PhD thesis, Ecole Centrale de Lyon, Lyon, France.
[17] Boudet, J., Caro, J., Shao, L., and Lévêque, E., 2007, "Numerical Studies Towards Practical Large-Eddy Simulation," J. Therm. Sci., **16**(4), pp. 328–336.
[18] Jameson, A., 1982, "Transonic Airfoil Calculations Using the Euler Equations," *Numerical Methods in Aeronautical Fluid Dynamics*, Vol. 1, Academic Press, New York, pp. 289–308.
[19] Sagaut, P., 2002, Large Eddy Simulation for Incompressible Flows, Springer, Berlin, Germany.
[20] Cahuzac, A., Boudet, J., Jacob, M. C., and Kausche, P., 2011, "Large-Eddy Simulation of a Rotor Tip-Clearance Flow," AIAA Paper No. 2011–2947.
[21] Menter, F. R., Kuntz, M., and Langtry, R., 2003, "Ten Years of Industrial Experience With the SST Turbulence Model," *Turbulence, Heat and Mass Transfer 4*, Begell House Inc., New York.
[22] Day, I. J., 2006, "The Fundamentals of Stall and Surge," *Advances in Axial Compressor Aerodynamics* (Lecture Series Monographs), von Karman Institute, Brussels, Belgium.
[23] Inoue, M., Kuroumaru, M., Tanino, T., Yoshida, S., and Furukawa, M., 2001, "Comparative Studies on Short and Long Length-Scale Stall Cell Propagating in an Axial Compressor Rotor," ASME J. Turbomach., **123**(1), p. 24.
[24] März, J., Hah, C., and Neise, W., 2002, "An Experimental and Numerical Investigation Into the Mechanisms of Rotating Instability," ASME J. Turbomach., **124**(3), p. 367.
[25] Zierke, W. C., Farrell, K. J., and Straka, W. A., 1995, "Measurements of the Tip Clearance Flow for a High-Reynolds-Number Axial-Flow Rotor," ASME J. Turbomach., **117**(4), pp. 522–532.
[26] Kameier, F., and Neise, W., 1997, "Experimental Study of Tip Clearance Losses and Noise in Axial Turbomachines and Their Reduction," ASME J. Turbomach., **119**(3), pp. 460–471.
[27] You, D., Wang, M., Moin, P., and Mittal, R., 2007, "Vortex Dynamics and Low-Pressure Fluctuations in the Tip-Clearance Flow," ASME J. Fluids Eng., **129**(8), p. 1002.
[28] Bailey, S. C. C., and Tavoularis, S., 2008, "Measurements of the Velocity Field of a Wing-Tip Vortex, Wandering in Grid Turbulence," J. Fluid Mech., **601**, pp. 281–315.